Supporting Information

FeCoNi nanoalloys embedded in hierarchical N-rich carbon matrix with enhanced oxygen electrocatalysis for rechargeable Zn-air batteries

Jinlong Liu,[*abd] Ziyu Luo,[a] Xinxin Zhang,[a] Hailong Zheng,[a] Lei Peng,[a] Dong Qian,[a] Chuankun Jia,[c] Dongxiao Sun-Waterhouse[b] and Geoffrey I. N. Waterhouse[*bd]

[a.] College of Chemistry and Chemical Engineering, Central South University, Changsha 410083, P. R. China.

[b.] School of Chemical Sciences, The University of Auckland, Auckland 1142, New Zealand .

[c.] College of Materials Science and Engineering, Changsha University of Science & Technology, Changsha 410114, P. R. China.

[d.] MacDiarmid Institute for Advanced Materials and Nanotechnology, Wellington 6140, New Zealand.

E-mail: * jinlong.liu@auckland.ac.nz; * g.waterhouse@auckland.ac.nz

1. Experimental Section

1.1 Synthesis of Materials

To synthesize FeCoNi@HNC, 5 mmol of $Fe(NO_3)_3 \cdot 9H_2O$, 5 mmol of $Co(NO_3)_2 \cdot 6H_2O$, and 5 mmol of $Ni(NO_3)_2 \cdot 6H_2O$ were dissolved in 50 mL of deionized water under magnetic stirring. Meanwhile, 66.6 mmol of urea and 11.9 mmol of dicyandiamide were dissolved in another 50 mL of deionized water under magnetic stirring. The two solutions were then mixed with vigorous stirring for 30 min. Afterwards, the mixed solution was frozen using liquid nitrogen, then dried by lyophilization. The obtained solid was subsequently heated (5 $^{o}C\ min^{-1}$) to 550 ^{o}C under a N_2 flow in a tube furnace, then annealed at 550 ^{o}C for 2 h. The product was then ground into a powder and mixed with zinc powder in a 1:1 mass ratio, after which the powder mixture was heated (2 $^{o}C\ min^{-1}$) to 900 ^{o}C under a N_2 flow in a tube furnace, then held at 900 ^{o}C for 1 h. The pyrolysis product was etched two times by immersion in 1 M HCl for 12 h, then washed with deionized water several times, and finally dried at 60 ^{o}C in a vacuum oven. For comparison, Fe@HNC, Co@HNC and Ni@HNC were also prepared by similar procedures, except that 15 mmol of $Fe(NO_3)_3 \cdot 9H_2O$, 15 mmol of $Co(NO_3)_2 \cdot 6H_2O$ and 15 mmol of $Ni(NO_3)_2 \cdot 6H_2O$, respectively, were used instead of a mixture of the three different metal nitrates.

1.2 Material Characterizations

The morphologies and microstructures of the synthesized samples were examined using a FEI Quanta 450 field-emission scanning electron microscope (FESEM) equipped with energy-dispersive X-ray spectroscopy detector and a Tecnai G2 60-300 HOLO transmission electron microscope (TEM) with image corrector. X-ray diffraction (XRD) patterns were recorded on a Bruker D8 Advance powder X-ray diffractometer with Cu Kα radiation. TGA analyses were performed on a TGA/DSC 2 STAR system under an air atmosphere. N_2 adsorption-desorption isotherms were collected on a Tristar 3000 surface area and pore analyzer (Micromeritics). X-ray photoelectron spectroscopy (XPS) data were collected on a Thermo Escalab 250Xi spectrometer equipped with a monochromatic Al Kα source.

1.3 Electrochemical Measurements

The catalyst powders were first characterized by the rotating disk electrode (RDE) method in a standard three-electrode system with 0.1 M KOH as the electrolyte using an electrochemical workstation (CHI 760E). Specifically, 2 mg of catalyst was dispersed in a mixed solution consisting of 500 μL of deionized water, 450 μL of ethanol and 50 μL of Nafion (5 wt.%) under sonication for 1 h. Then 10 μL of the catalyst ink was loaded onto a glassy carbon RDE (diameter = 5 mm), with the modified electrode then dried naturally in the air. This served as the working electrode. A Pt plate and Hg/HgO electrode were employed as the counter electrode and reference electrode, respectively. The 0.1 M KOH electrolyte was purged by a flow of pure O_2 for 30 min prior to electrochemical testing, with the O_2 purge being maintained during the electrochemical measurements. Linear sweep voltammetry (LSV) at a slow scan rate of 5 mV s^{-1} was adopted to investigate the ORR/OER polarization behaviour of the catalysts. Cyclic voltammetry (CV) was employed to probe the cycling stability and electrochemically active areas of the catalysts. All potentials were referenced to a reversible hydrogen electrode by adding a value of (0.098 + 0.0592×pH).

The electron transfer number was calculated according to the Koutecky-Levich equation:[1]

$$\frac{1}{J} = \frac{1}{J_L} + \frac{1}{J_K} = \frac{1}{B}\omega^{-\frac{1}{2}} + \frac{1}{J_K}$$

$$B = 0.62nFC_0D_0^{\frac{2}{3}}V^{-\frac{1}{6}}$$

where J, J_K and J_L are the measured current density, kinetic current density and limiting current density, respectively, ω is the rotational speed of the RDE, n is the overall number of electrons transferred in ORR, F is the Faraday constant, C_0 is the saturated O_2 concentration in the electrolyte, D_0 is the O_2 diffusion coefficient, and V is the viscosity of the electrolyte.

1.4 Zinc-air battery measurements

Zinc-air batteries were assembled using the catalyst-loaded carbon cloth as the air electrode, a zinc plate as the metal electrode, and a mixed aqueous solution containing 6.0 M KOH and 0.2 M $Zn(Ac)_2$ as the electrolyte. The loading amount of FeCoNi@HNC catalyst on the carbon cloth was 1 mg cm^{-2}. For comparison, a mixture of commercial Pt/C and IrO_2/C catalysts (mass ratio of 1:1) was also loaded on carbon cloth (total loading 1 mg cm^{-2}) and evaluated as the air electrode in a rechargeable Zn-air battery. The performance of assembled zinc-air batteries was measured on an electrochemical workstation (CHI 760E) at the room temperature.

1.5 Computation methods

Spin-polarized density functional theory (DFT) calculations were performed using the Vienna ab initio Simulation Package (VASP).[2, 3] The core electrons were described using the projected augmented wave (PAW) method,[4, 5] and the electron interactions were treated by the Perdew-Burke-Ernzerhof (PBE) exchange-correlation functional within the generalized gradient approximation (GGA),[6] with a plane-wave cutoff energy of 600 eV. The dispersion correction in Grimme's scheme was considered using DFT-D3 method.[7] The Brillouin zone was sampled with Γ-point-centered Monkhorst-Pack k-point grid of 2×2×2 for $Fe_2Co_2Ni_2@C_{74}N_8$, 3×3×1 for Pt(111) and IrO_2(110), 3×3×1 for N-rich graphene ($C_{54}N_6$), 1×1×3 for a N-rich carbon nanotube ($C_{108}N_{12}$), respectively. The energy and force convergence thresholds were set to be 1×10^{-5} eV and 0.02 eV $Å^{-1}$, respectively. For the calculation of density of states, the k-point grid was increased to 6×6×6 for $Fe_2Co_2Ni_2@C_{74}N_8$, 12×12×1 for Pt(111) and IrO_2(110), 12×12×1 for N-rich graphene ($C_{54}N_6$), 1×1×12 for N-rich carbon nanotube ($C_{108}N_{12}$), respectively. A vacuum space of 15 Å in the *a*, *b* and *c* directions for $Fe_2Co_2Ni_2@C_{74}N_8$, *c* direction for Pt(111), IrO_2(110), and N-rich graphene ($C_{54}N_6$), *a* and *b* directions for N-rich carbon nanotube ($C_{108}N_{12}$) was applied to avoid interactions between mirror images.

Under the alkaline conditions (e.g., 0.1 M KOH, pH = 13), the four-electron mechanism of ORR involves the following steps:[8]

$$* + O_2 \rightarrow *O_2 \quad (1)$$

$$*O_2 + H_2O + e^- \rightarrow *OOH + OH^- \quad (2)$$

$$*OOH + e^- \rightarrow *O + OH^- \quad (3)$$

$$*O + H_2O + e^- \rightarrow *OH + OH^- \quad (4)$$

$*OH + e^- \rightarrow * + OH^-$ (5)

As the reverse reaction of ORR, OER occurs via the following processes:[9]

$* + OH^- \rightarrow *OH + e^-$ (6)

$*OH + OH^- \rightarrow *O + H_2O + e^-$ (7)

$*O + OH^- \rightarrow *OOH + e^-$ (8)

$*OOH + OH^- \rightarrow *O_2 + H_2O + e^-$ (9)

$*O_2 \rightarrow * + O_2$ (10)

where * denotes the adsorption site for oxygen-containing intermediates. The free energy for the elementary reaction step was calculated using the following equation:[10-12]

$\Delta G = \Delta E + \Delta ZPE - T\Delta S + \Delta G_{pH} + \Delta G_U + \Delta G_{sol}$ (11)

Where ΔE is the electronic energy difference, ΔZPE is the zero-point energy (ZPE) correction, T is the thermodynamic temperature (here T = 298.15 K), ΔS is the entropy change, ΔG_{pH} is the correction for H^+ free energy ($\Delta G_{pH} = 0.0592 \times pH$), ΔG_U is the energy change originated from the applied potential U ($\Delta G_U = -neU$, where n is the number of electron transferred, and e is the elementary electric charge), and ΔG_{sol} is the correction caused by solvent effect (0.50 eV for direct OH adsorption).[10, 12] To calculate the free energy diagrams, the concept of the computational hydrogen electrode (CHE) proposed by Nørskov et al. was adopted, that is, the chemical potential of the proton-electro pair ($H^+ + e^-$) equals $1/2H_2$ in the electrolyte with pH = 0 and 1 bar of H_2 in the gas at 298.15 K.[8] ΔZPE and ΔS were calculated from the vibrational frequency analysis of adsorption species. Specifically, $ZPE = \sum \frac{h\upsilon}{2}$, and $S = \sum R\{\frac{\beta h\upsilon}{e^{\beta h\upsilon}-1} - \ln(1 - e^{\beta h\upsilon})\}$, where h is Planck's constant, υ is the vibrational frequencies of adsorbed species, R is gas constant, $\beta = \frac{1}{k_B T}$, and e is mathematical constant.

The difference charge density of $Fe_2Co_2Ni_2@C_{74}N_8$ was calculated based on the following equation:

$\Delta\rho = \rho(Fe_2Co_2Ni_2@C_{74}N_8) - \rho(Fe_2Co_2Ni_2) - \rho(C_{74}N_8)$ (12)

2. Supplementary Figures

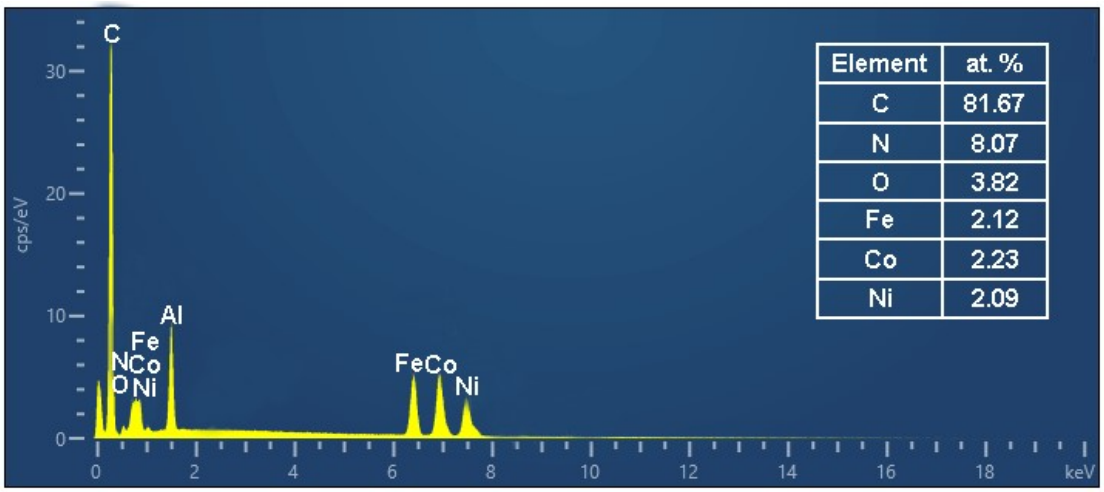

Fig. S1 EDX spectrum of FeCoNi@HNC.

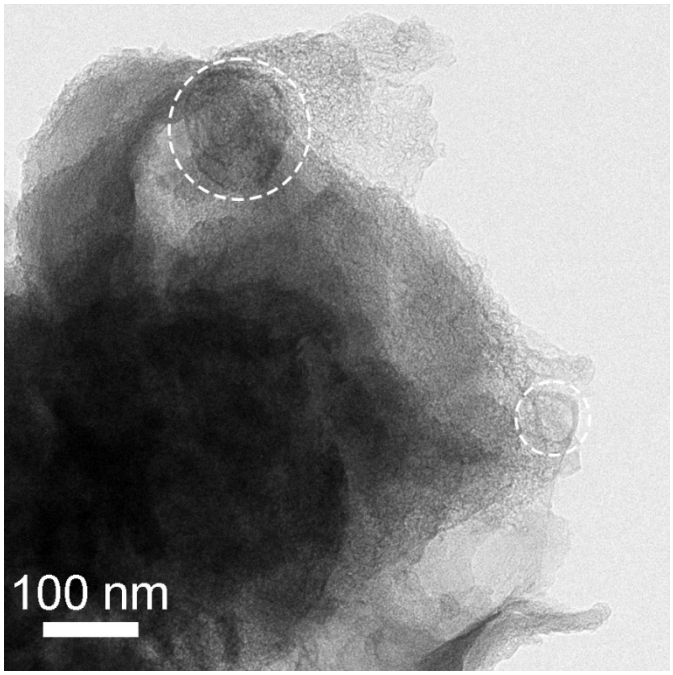

Fig. S2 Graphene network of FeCoNi@HNC after the acid treatment. The selected areas show the cavities created by the removal of FeCoNi nanoalloy nanoparticles.

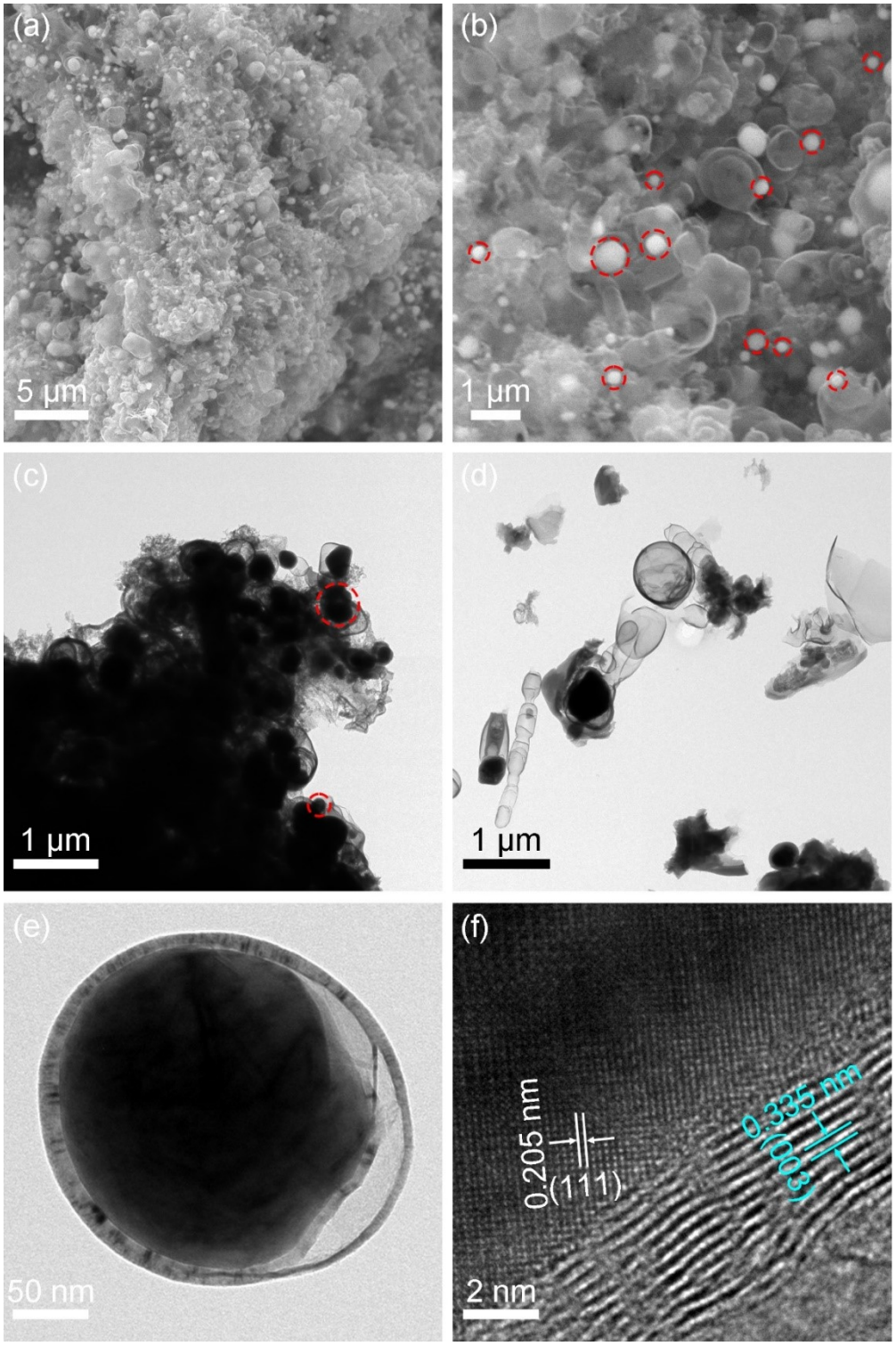

Fig. S3 (a,b) SEM, (c−e) TEM, and (f) HRTEM images of FeCoNi@HNC before acid etching. The selected areas in panel (b) and (c) show some FeCoNi nanoparticles without carbon coating.

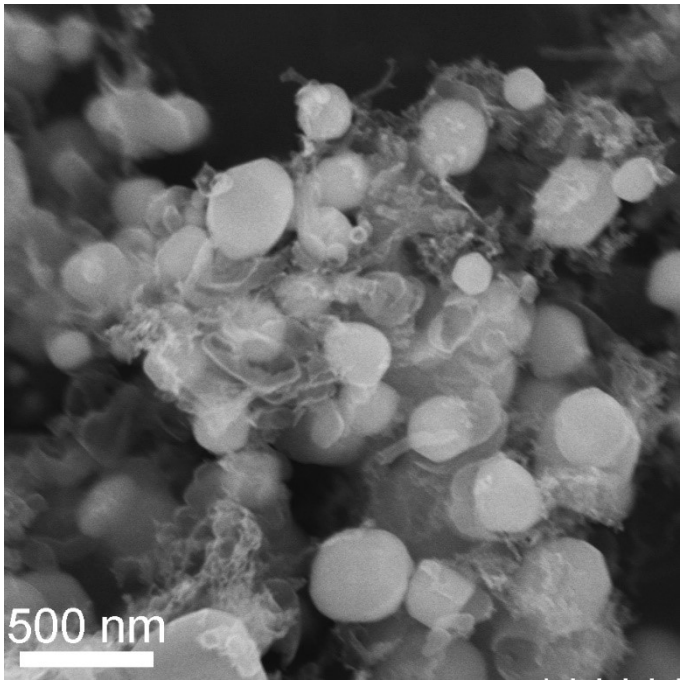

Fig. S4. Representative SEM image of Fe@HNC.

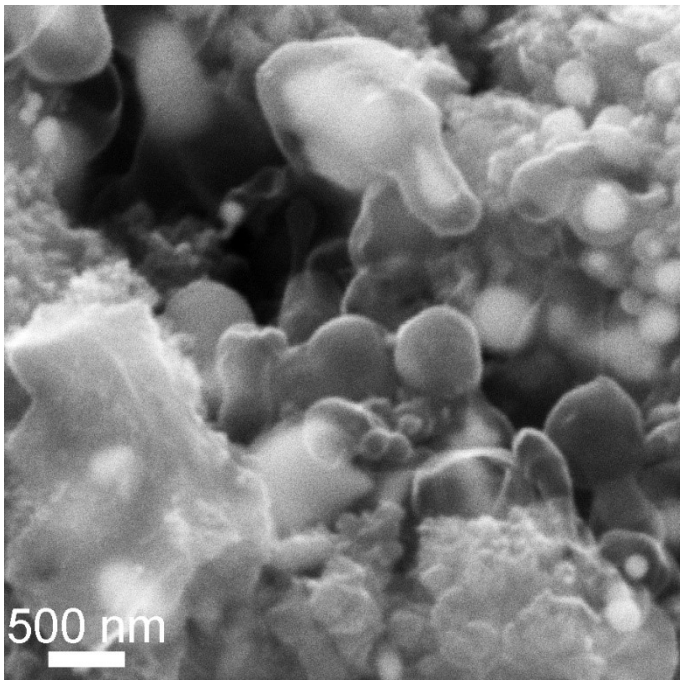

Fig. S5 Representative SEM image of Co@HNC.

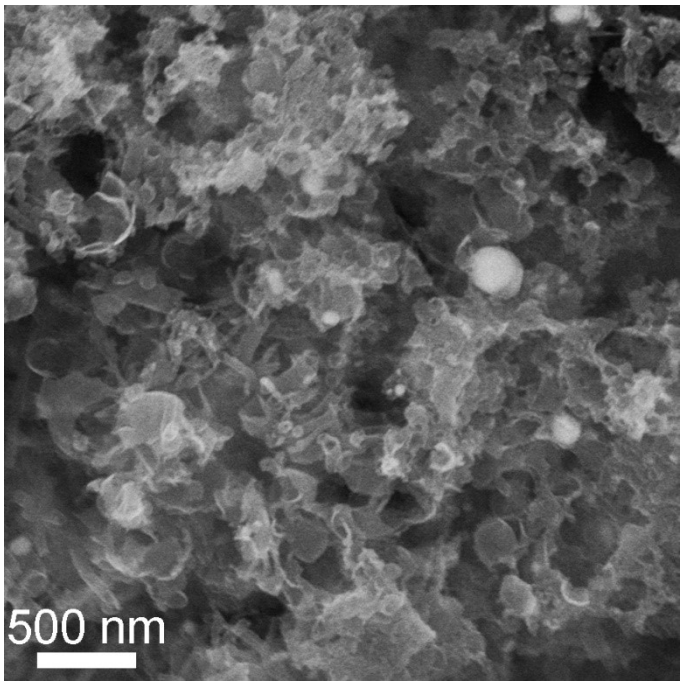

Fig. S6 Representative SEM image of Ni@HNC.

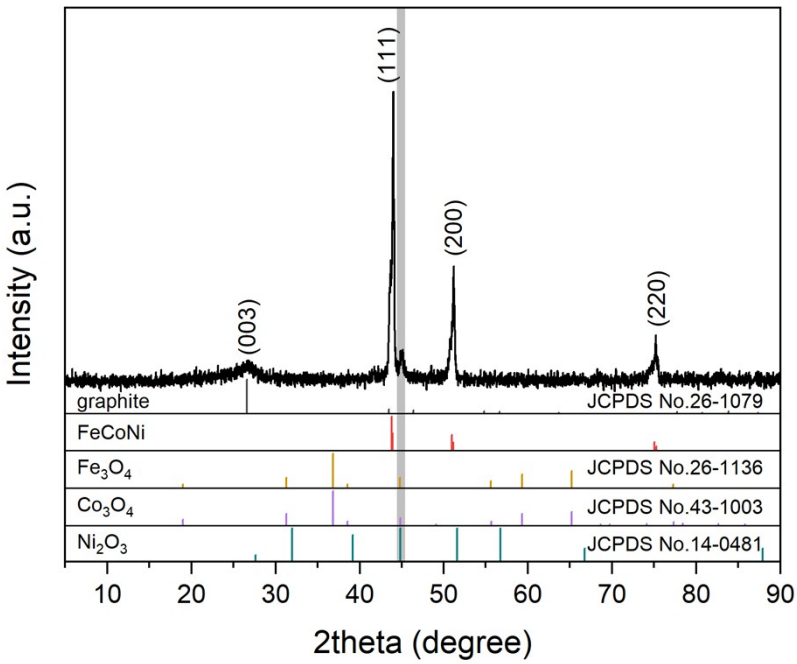

Fig. S7 XRD pattern of FeCoNi@HNC before acid etching.

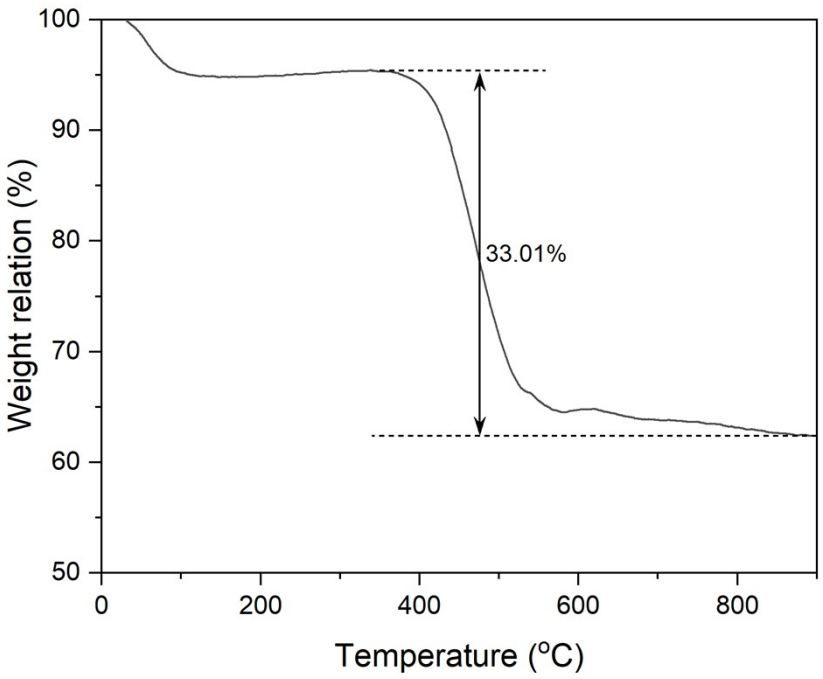

Fig. S8 TGA curve of FeCoNi@HNC before acid etching.

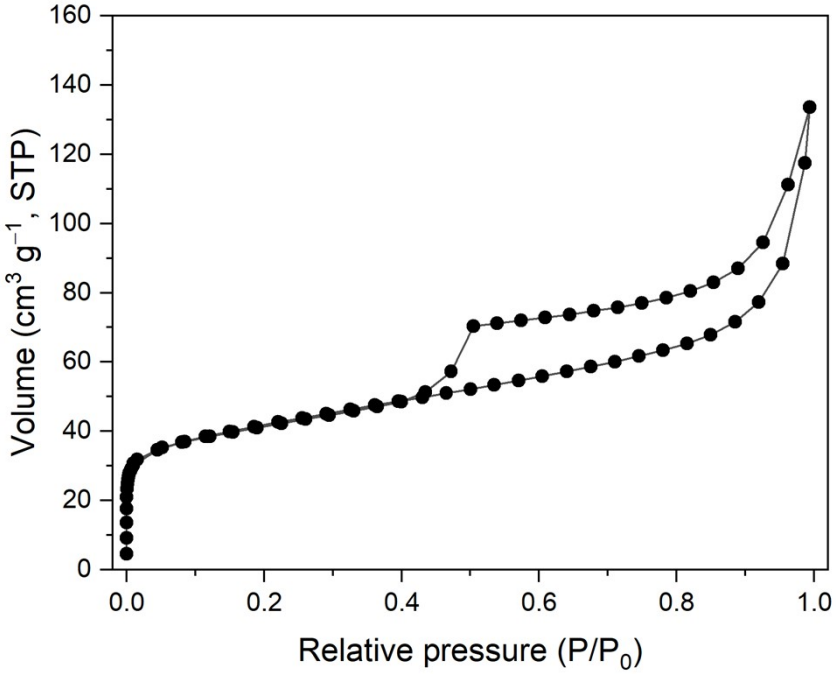

Fig. S9 N_2 adsorption and desorption isotherms for FeCoNi@HNC before acid etching.

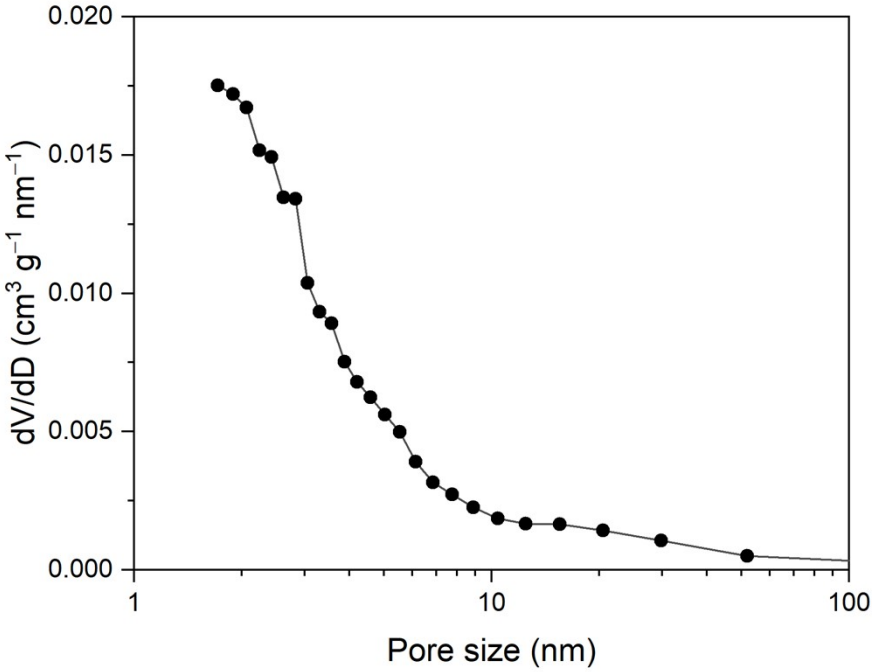

Fig. S10 Pore size distribution of FeCoNi@HNC before acid etching.

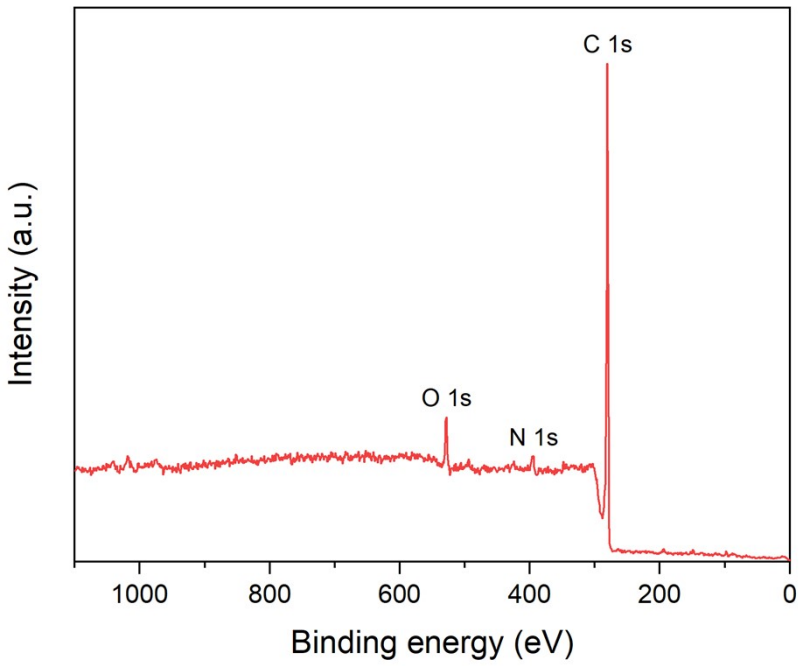

Fig. S11 Survey XPS spectrum of FeCoNi@HNC after acid etching.

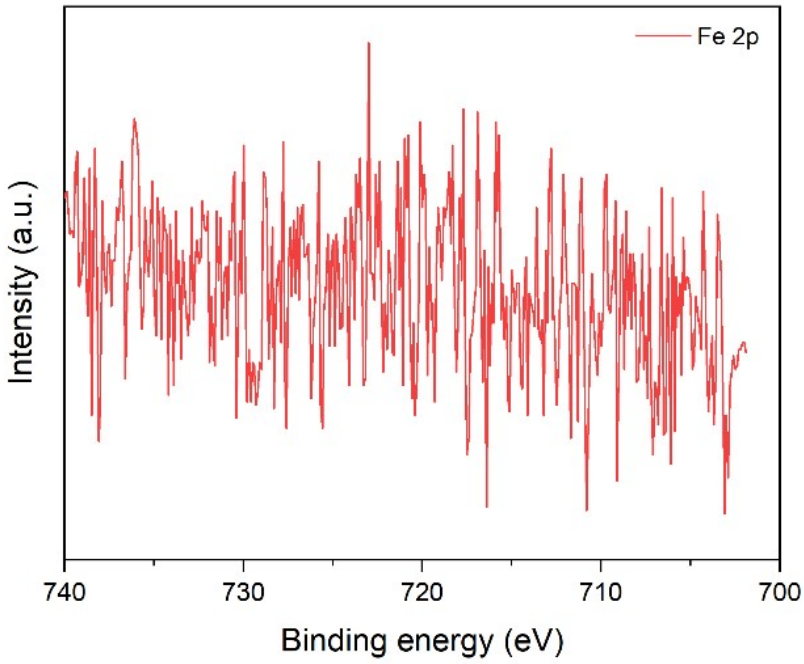

Fig. S12 High-resolution Fe 2p XPS spectrum for FeCoNi@HNC after acid etching.

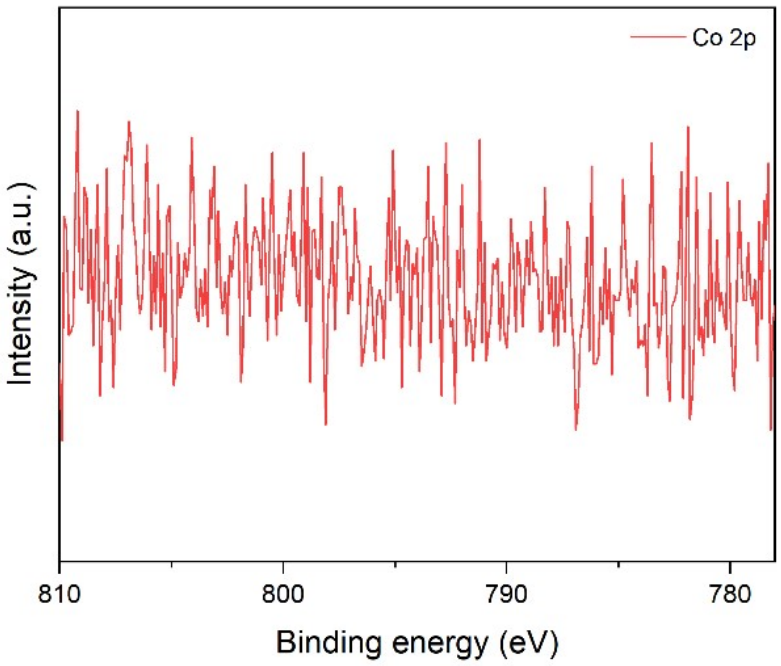

Fig. S13 High-resolution Co 2p XPS spectrum for FeCoNi@HNC after acid etching.

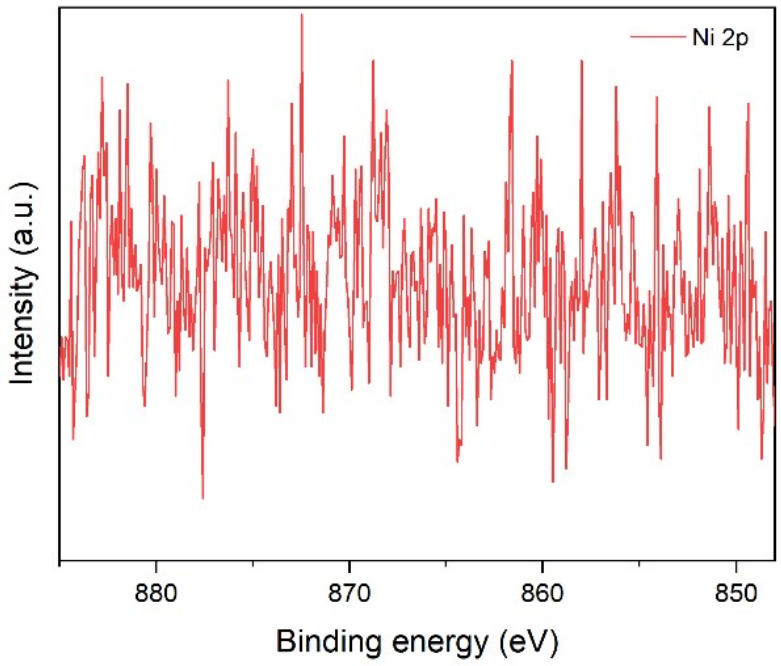

Fig. S14 High-resolution Ni 2p XPS spectrum for FeCoNi@HNC after acid etching.

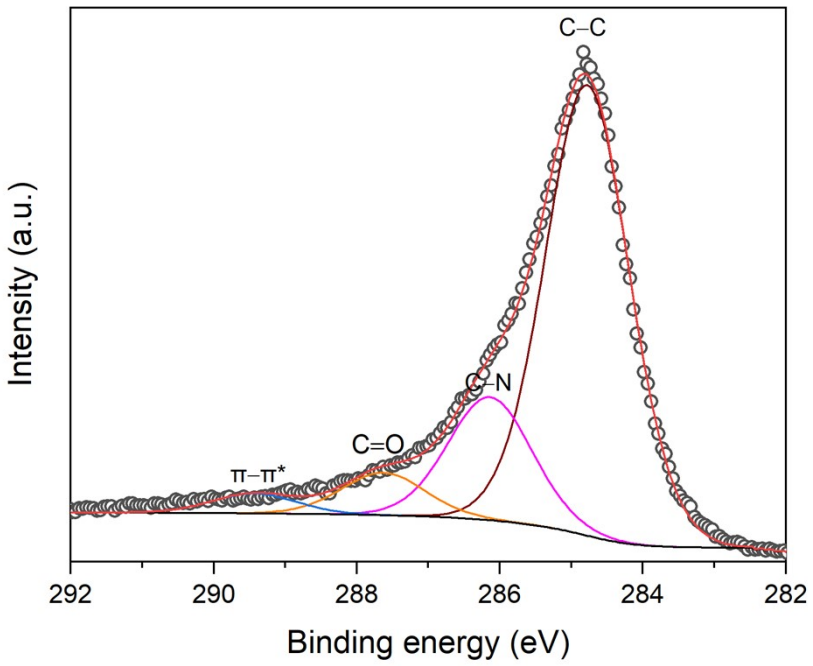

Fig. S15 High-resolution C 1s XPS spectrum for FeCoNi@HNC before acid etching.

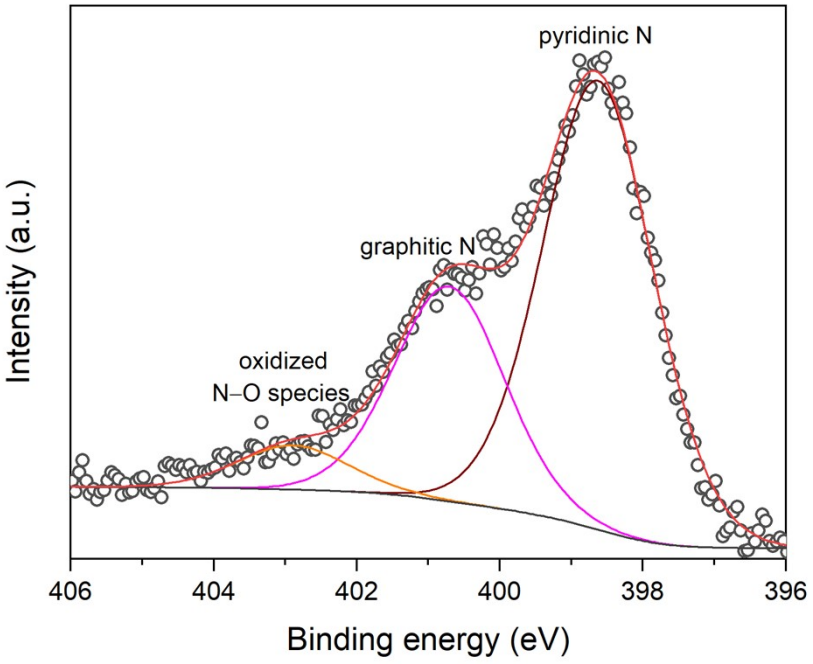

Fig. S16 High-resolution N 1s XPS spectrum for FeCoNi@HNC before acid etching.

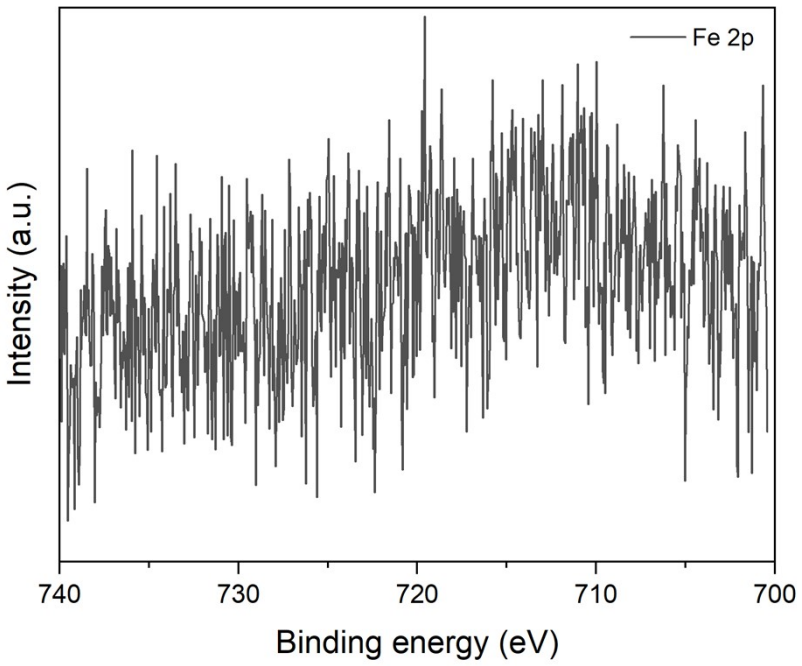

Fig. S17 High-resolution Fe 2p XPS spectrum for FeCoNi@HNC before acid etching.

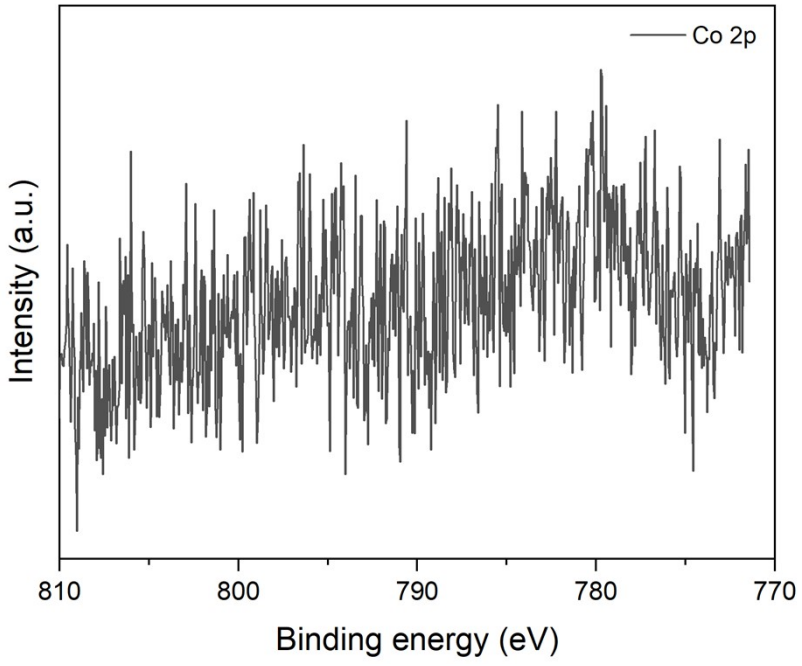

Fig. S18 High-resolution Co 2p XPS spectrum for FeCoNi@HNC before acid etching.

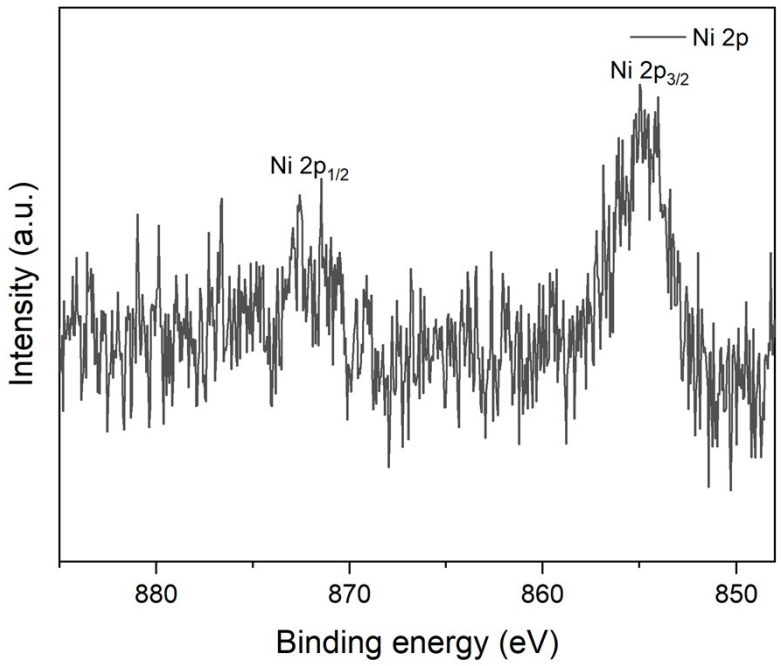

Fig. S19 High-resolution Ni 2p XPS spectrum for FeCoNi@HNC before acid etching.

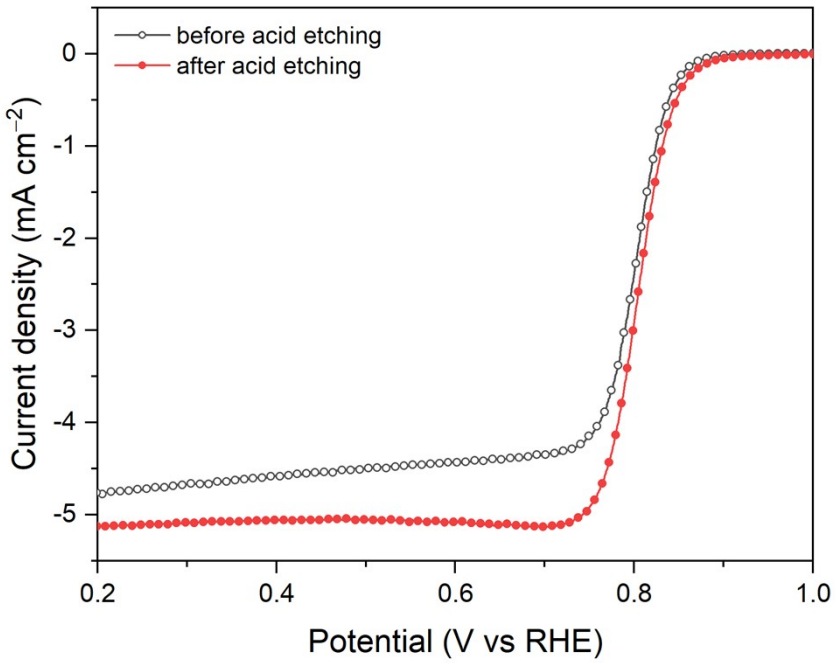

Fig. S20 ORR polarization curves for FeCoNi@HNC before and after acid etching.

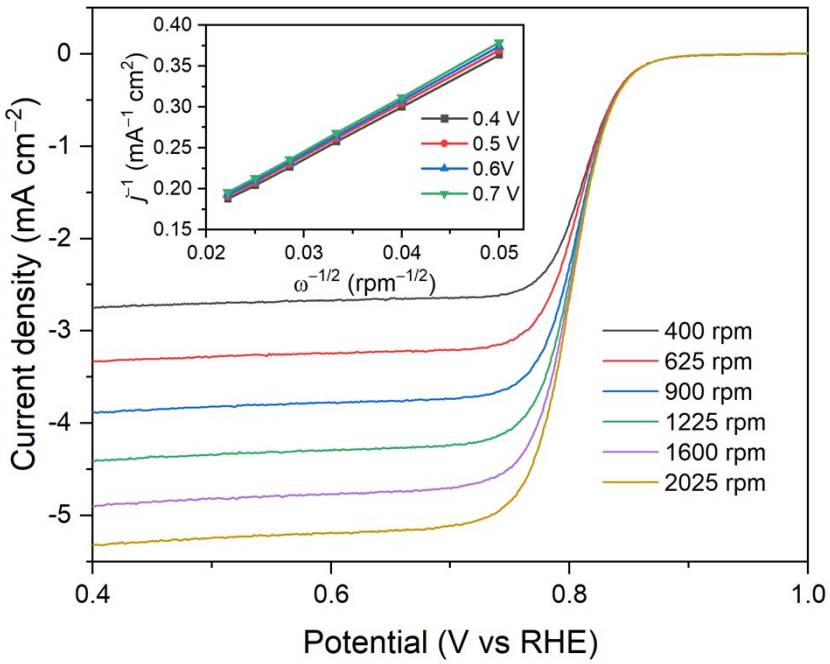

Fig. S21 ORR polarization curves for FeCoNi@HNC at different rotation rates.

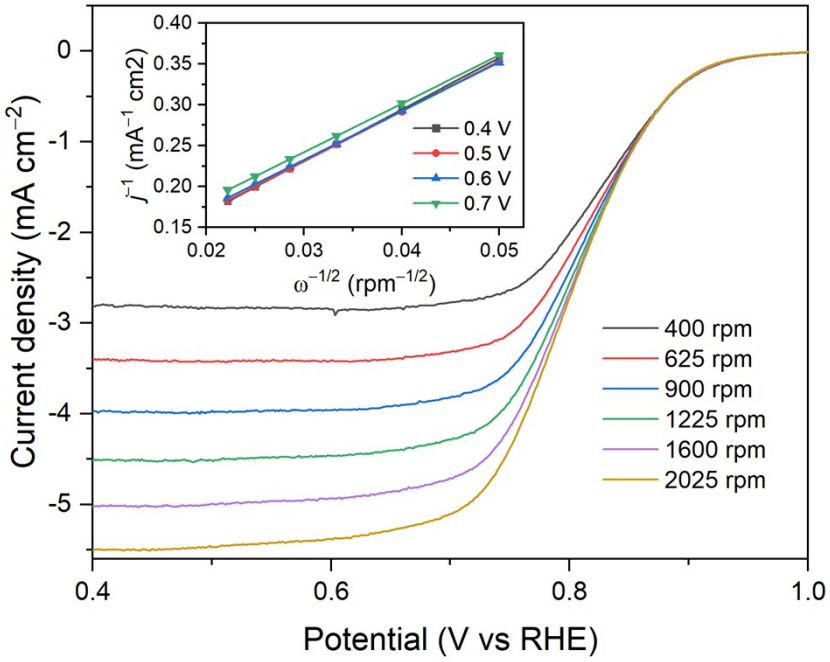

Fig. S22 ORR polarization curves for commercial 20 wt.% Pt/C at different rotation rates.

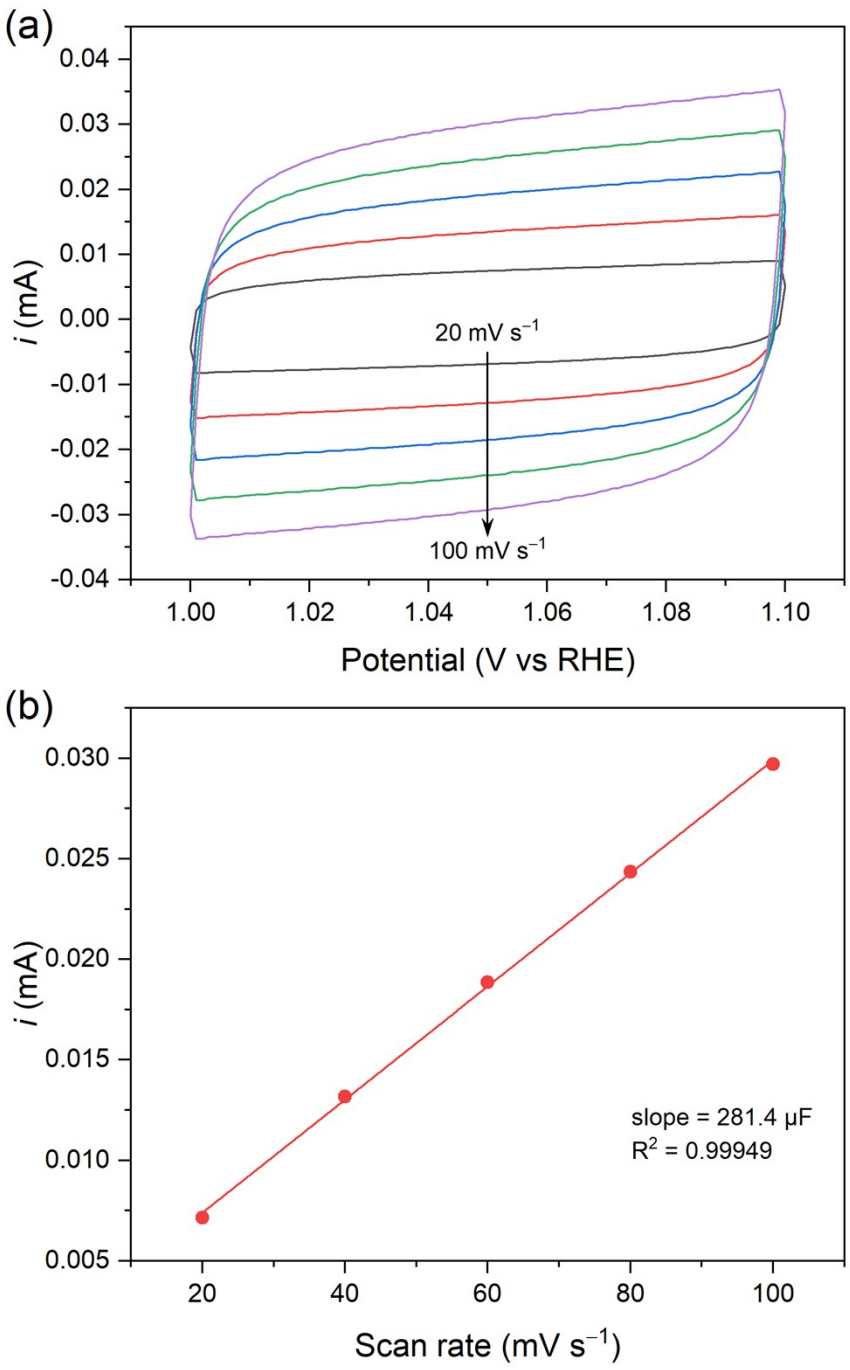

Fig. S23 (a) CV curves, and (b) capacitive currents at 1.05 V vs RHE against scan rate for FeCoNi@HNC.

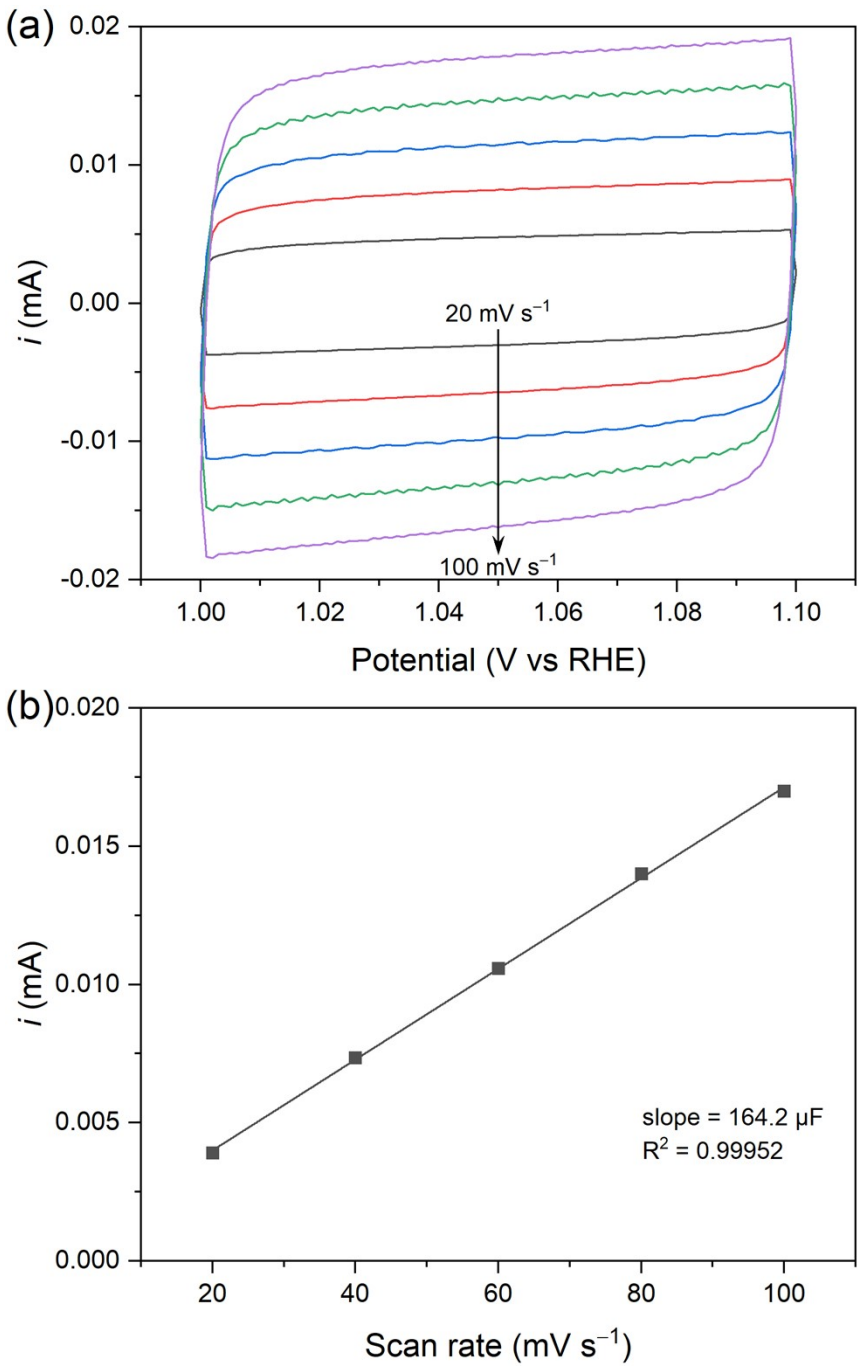

Fig. S24 (a) CV curves, and (b) capacitive currents at 1.05 V vs RHE against scan rate for commercial 20 wt.% Pt/C.

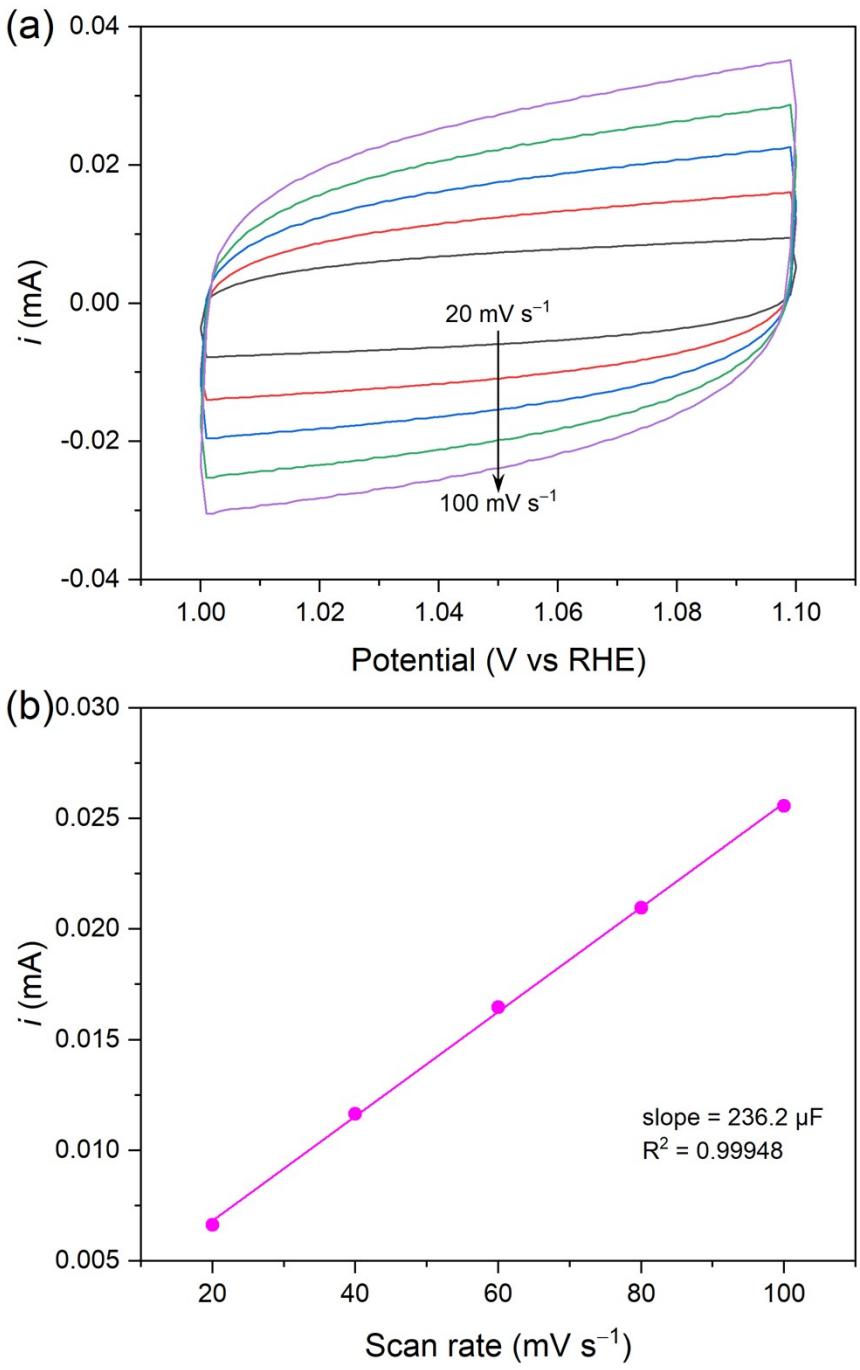

Fig. S25 (a) CV curves, and (b) the capacitive currents at 1.05 V vs RHE against scan rate of FeCoNi@HNC before acid etching.

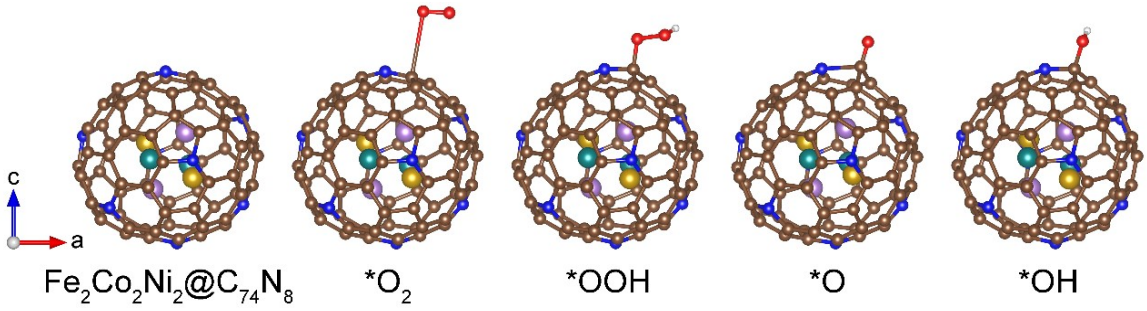

Fig. S26 Atomic configurations of optimized $Fe_2Co_2Ni_2@C_{74}N_8$ model and oxygen intermediates, where brown, blue, red, white, yellow, purple, and green spheres represent C, N, O, H, Fe, Co, and Ni atoms, respectively.

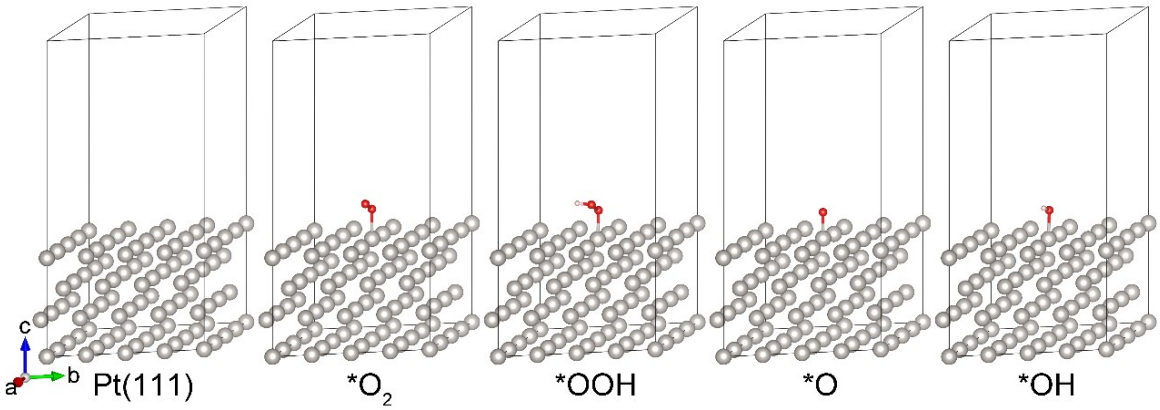

Fig. S27 Atomic configurations of optimized Pt(111) model and oxygen intermediates, where gray, red, and white spheres represent Pt, O, and H atoms, respectively.

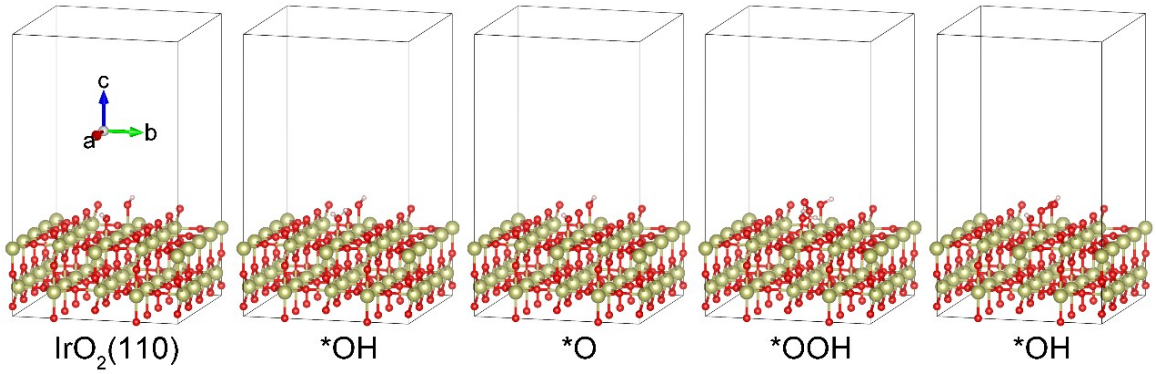

Fig. S28 Atomic configurations of optimized $IrO_2(110)$ model and oxygen intermediates, where yellow, red, and white spheres represent Ir, O, and H atoms, respectively.

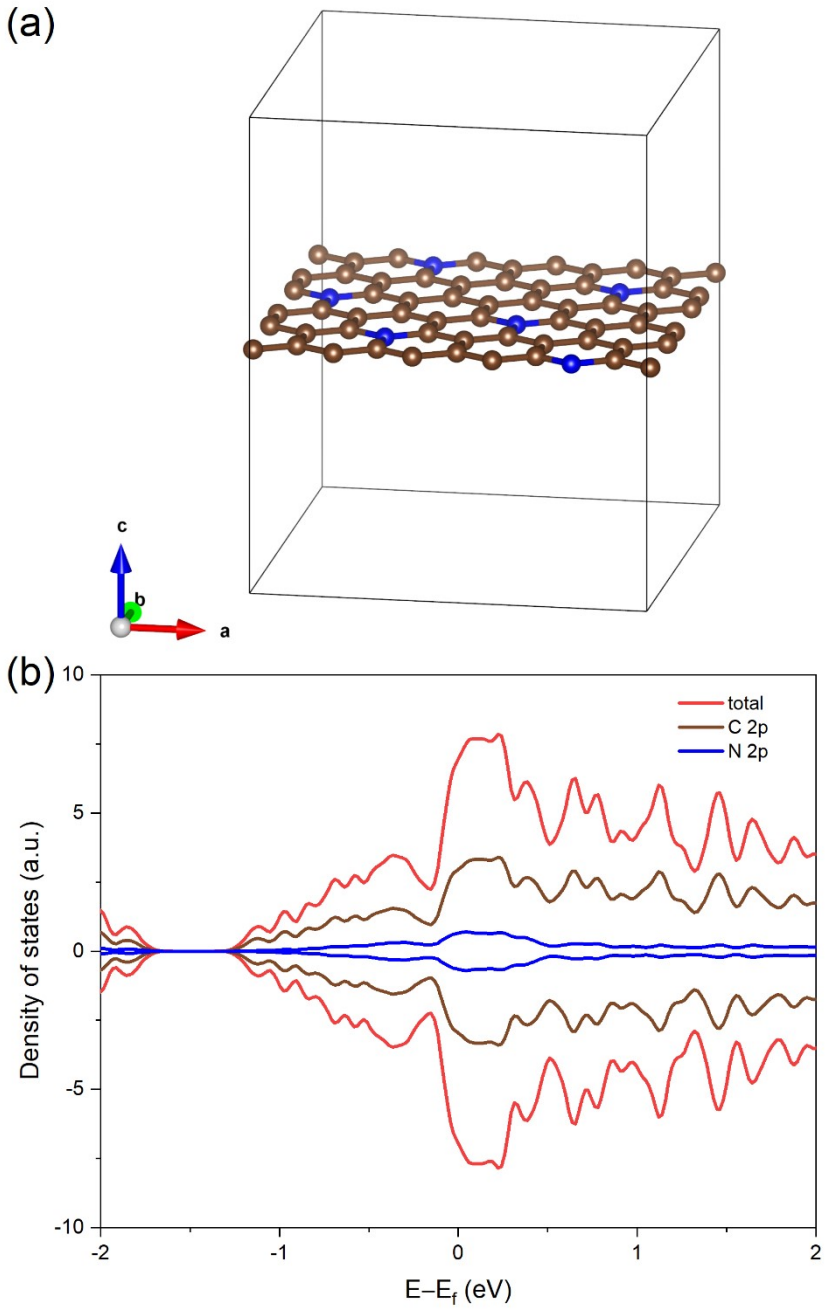

Fig. S29 (a) Atomic configuration and (b) DOS of N-rich graphene ($C_{54}N_6$).

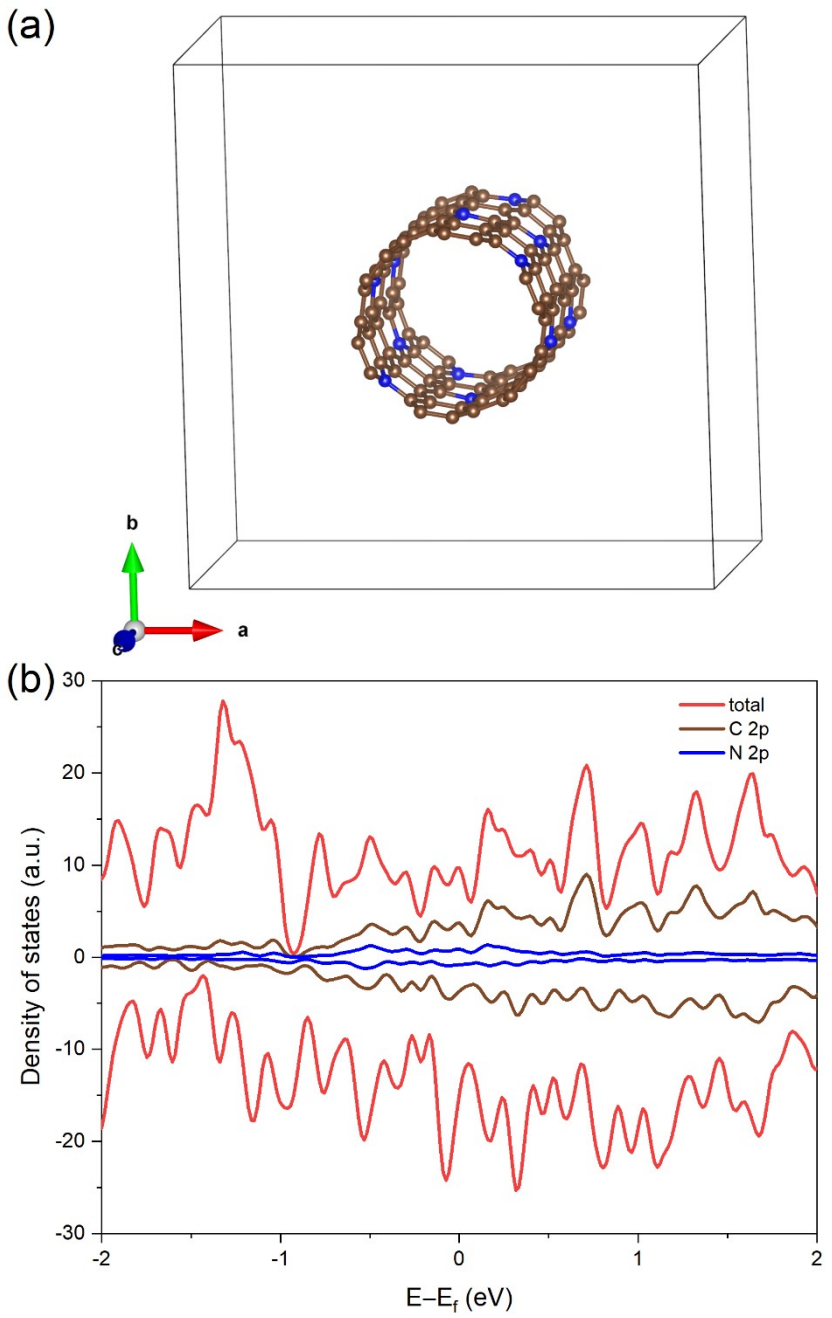

Fig. S30 (a) Atomic configuration and (b) DOS of N-rich CNT ($C_{108}N_{12}$).

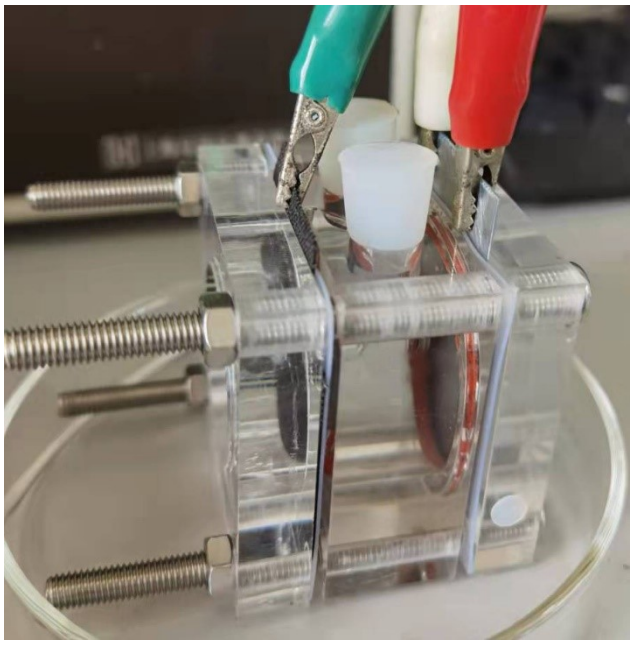

Fig. S31 Photograph of prototype zinc-air battery. The air electrode is on the left, zinc plate electrode on the right.

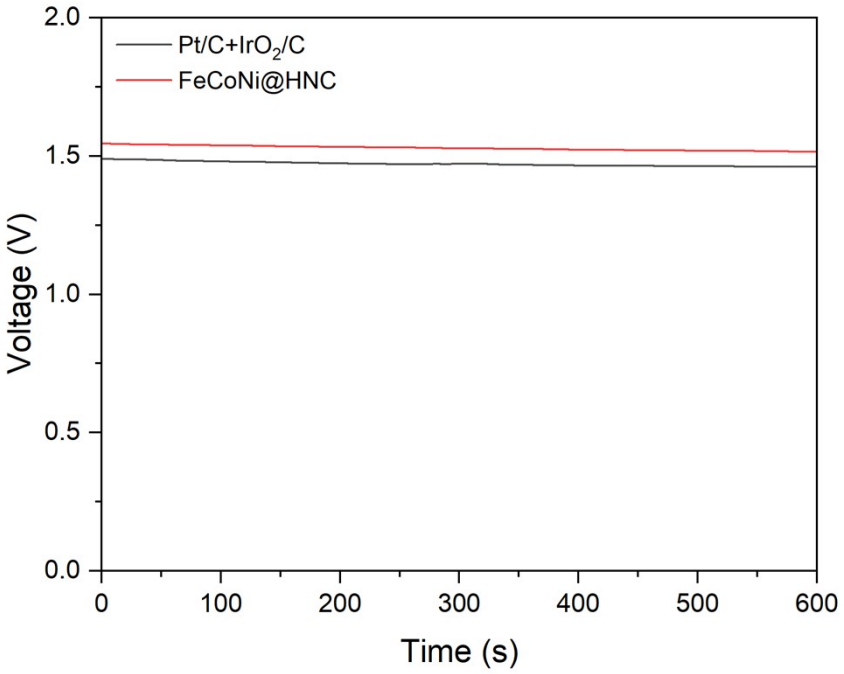

Fig. S32 Open-circuit voltage of zinc-air batteries fabricated using FeCoNi@HNC and Pt/C+IrO_2/C as the air electrode catalysts.

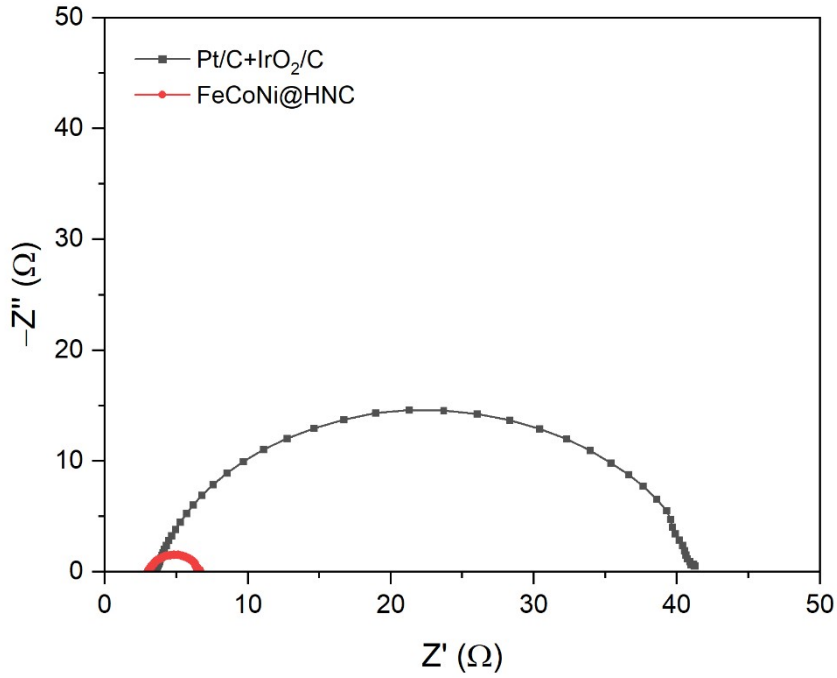

Fig. S33 Nyquist plots of ZABs fabricated using FeCoNi@HNC and Pt/C+IrO_2/C as the air electrode catalysts.

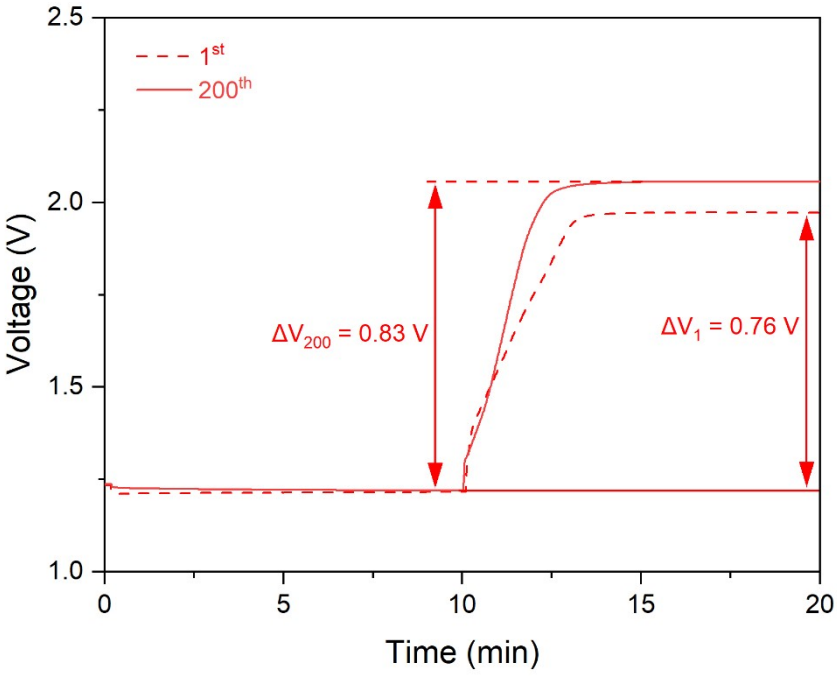

Fig. S34 The 1st and 200th galvanostatic discharge-charge curves of ZAB driven by the FeCoNi@HNC catalyst at a current density of 5 mA cm^{-2}.

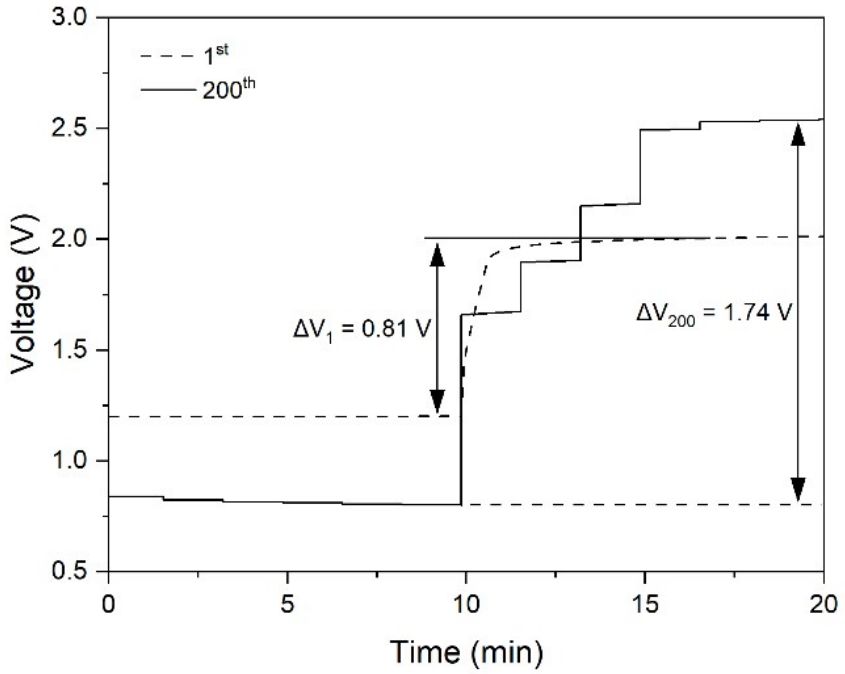

Fig. S35 The 1st and 200th galvanostatic discharge-charge curves of ZAB driven by the Pt/C+IrO_2/C catalyst at a current density of 5 mA cm^{-2}.

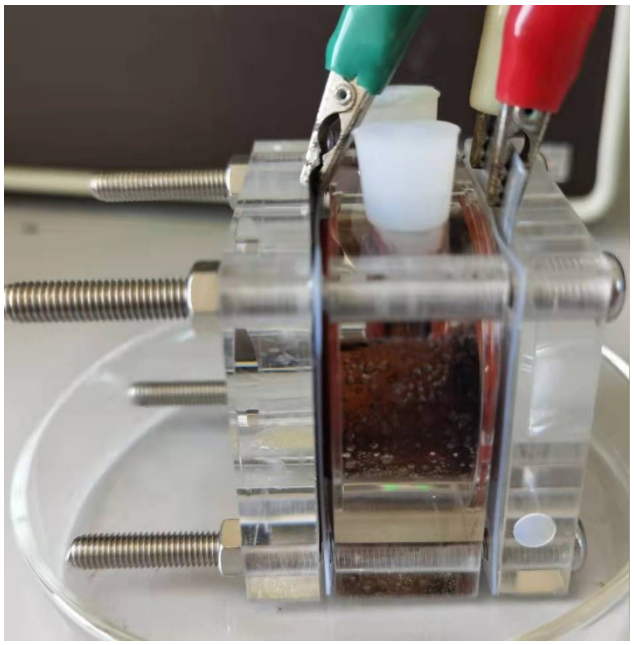

Fig. S36 Photograph of zinc-air battery fabricated using Pt/C+IrO_2/C as the air electrode catalysts after 200 cycles.

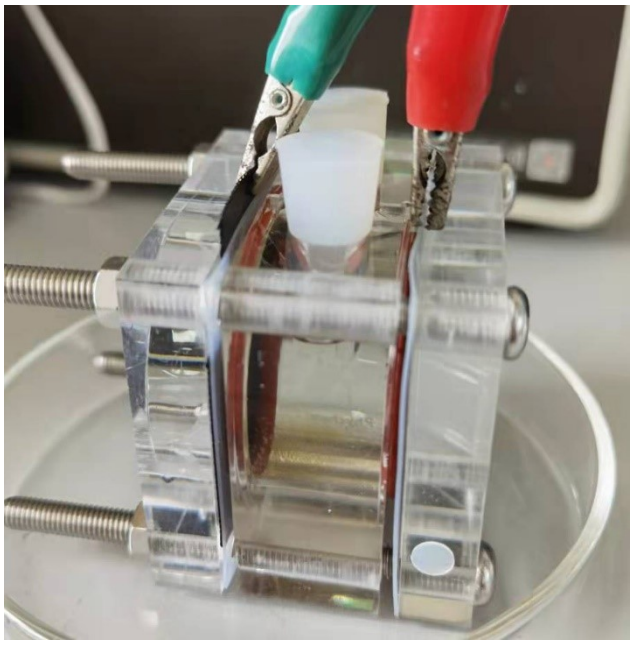

Fig. S37 Photograph of zinc-air battery fabricated using FeCoNi@HNC as air electrode catalyst after 200 cycles.

3. Supplementary Notes

Note 1. CIF of FeCoNi alloy

```
#======================================================================
# CRYSTAL DATA
#----------------------------------------------------------------------
data_VESTA_phase_1

_chemical_name_common                  'Co0.027 Fe0.283 Ni0.689'
_cell_length_a                         3.577696
_cell_length_b                         3.577696
_cell_length_c                         3.577696
_cell_angle_alpha                      90.000000
_cell_angle_beta                       90.000000
_cell_angle_gamma                      90.000000
_cell_volume                           45.794185
_space_group_name_H-M_alt              'F m -3 m'
_space_group_IT_number                 225

loop_
_space_group_symop_operation_xyz
   'x, y, z'
   '-x, -y, -z'
   '-x, -y, z'
   'x, y, -z'
   '-x, y, -z'
   'x, -y, z'
   'x, -y, -z'
   '-x, y, z'
   'z, x, y'
   '-z, -x, -y'
   'z, -x, -y'
   '-z, x, y'
   '-z, -x, y'
   'z, x, -y'
   '-z, x, -y'
   'z, -x, y'
   'y, z, x'
   '-y, -z, -x'
   '-y, z, -x'
   'y, -z, x'
   'y, -z, -x'
   '-y, z, x'
   '-y, -z, x'
   'y, z, -x'
   'y, x, -z'
```

'-y, -x, z'
'-y, -x, -z'
'y, x, z'
'y, -x, z'
'-y, x, -z'
'-y, x, z'
'y, -x, -z'
'x, z, -y'
'-x, -z, y'
'-x, z, y'
'x, -z, -y'
'-x, -z, -y'
'x, z, y'
'x, -z, y'
'-x, z, -y'
'z, y, -x'
'-z, -y, x'
'z, -y, x'
'-z, y, -x'
'-z, y, x'
'z, -y, -x'
'-z, -y, -x'
'z, y, x'
'x, y+1/2, z+1/2'
'-x, -y+1/2, -z+1/2'
'-x, -y+1/2, z+1/2'
'x, y+1/2, -z+1/2'
'-x, y+1/2, -z+1/2'
'x, -y+1/2, z+1/2'
'x, -y+1/2, -z+1/2'
'-x, y+1/2, z+1/2'
'z, x+1/2, y+1/2'
'-z, -x+1/2, -y+1/2'
'z, -x+1/2, -y+1/2'
'-z, x+1/2, y+1/2'
'-z, -x+1/2, y+1/2'
'z, x+1/2, -y+1/2'
'-z, x+1/2, -y+1/2'
'z, -x+1/2, y+1/2'
'y, z+1/2, x+1/2'
'-y, -z+1/2, -x+1/2'
'-y, z+1/2, -x+1/2'
'y, -z+1/2, x+1/2'
'y, -z+1/2, -x+1/2'
'-y, z+1/2, x+1/2'
'-y, -z+1/2, x+1/2'

'y, z+1/2, -x+1/2'
'y, x+1/2, -z+1/2'
'-y, -x+1/2, z+1/2'
'-y, -x+1/2, -z+1/2'
'y, x+1/2, z+1/2'
'y, -x+1/2, z+1/2'
'-y, x+1/2, -z+1/2'
'-y, x+1/2, z+1/2'
'y, -x+1/2, -z+1/2'
'x, z+1/2, -y+1/2'
'-x, -z+1/2, y+1/2'
'-x, z+1/2, y+1/2'
'x, -z+1/2, -y+1/2'
'-x, -z+1/2, -y+1/2'
'x, z+1/2, y+1/2'
'x, -z+1/2, y+1/2'
'-x, z+1/2, -y+1/2'
'z, y+1/2, -x+1/2'
'-z, -y+1/2, x+1/2'
'z, -y+1/2, x+1/2'
'-z, y+1/2, -x+1/2'
'-z, y+1/2, x+1/2'
'z, -y+1/2, -x+1/2'
'-z, -y+1/2, -x+1/2'
'z, y+1/2, x+1/2'
'x+1/2, y, z+1/2'
'-x+1/2, -y, -z+1/2'
'-x+1/2, -y, z+1/2'
'x+1/2, y, -z+1/2'
'-x+1/2, y, -z+1/2'
'x+1/2, -y, z+1/2'
'x+1/2, -y, -z+1/2'
'-x+1/2, y, z+1/2'
'z+1/2, x, y+1/2'
'-z+1/2, -x, -y+1/2'
'z+1/2, -x, -y+1/2'
'-z+1/2, x, y+1/2'
'-z+1/2, -x, y+1/2'
'z+1/2, x, -y+1/2'
'-z+1/2, x, -y+1/2'
'z+1/2, -x, y+1/2'
'y+1/2, z, x+1/2'
'-y+1/2, -z, -x+1/2'
'-y+1/2, z, -x+1/2'
'y+1/2, -z, x+1/2'
'y+1/2, -z, -x+1/2'

'-y+1/2, z, x+1/2'
'-y+1/2, -z, x+1/2'
'y+1/2, z, -x+1/2'
'y+1/2, x, -z+1/2'
'-y+1/2, -x, z+1/2'
'-y+1/2, -x, -z+1/2'
'y+1/2, x, z+1/2'
'y+1/2, -x, z+1/2'
'-y+1/2, x, -z+1/2'
'-y+1/2, x, z+1/2'
'y+1/2, -x, -z+1/2'
'x+1/2, z, -y+1/2'
'-x+1/2, -z, y+1/2'
'-x+1/2, z, y+1/2'
'x+1/2, -z, -y+1/2'
'-x+1/2, -z, -y+1/2'
'x+1/2, z, y+1/2'
'x+1/2, -z, y+1/2'
'-x+1/2, z, -y+1/2'
'z+1/2, y, -x+1/2'
'-z+1/2, -y, x+1/2'
'z+1/2, -y, x+1/2'
'-z+1/2, y, -x+1/2'
'-z+1/2, y, x+1/2'
'z+1/2, -y, -x+1/2'
'-z+1/2, -y, -x+1/2'
'z+1/2, y, x+1/2'
'x+1/2, y+1/2, z'
'-x+1/2, -y+1/2, -z'
'-x+1/2, -y+1/2, z'
'x+1/2, y+1/2, -z'
'-x+1/2, y+1/2, -z'
'x+1/2, -y+1/2, z'
'x+1/2, -y+1/2, -z'
'-x+1/2, y+1/2, z'
'z+1/2, x+1/2, y'
'-z+1/2, -x+1/2, -y'
'z+1/2, -x+1/2, -y'
'-z+1/2, x+1/2, y'
'-z+1/2, -x+1/2, y'
'z+1/2, x+1/2, -y'
'-z+1/2, x+1/2, -y'
'z+1/2, -x+1/2, y'
'y+1/2, z+1/2, x'
'-y+1/2, -z+1/2, -x'
'-y+1/2, z+1/2, -x'

```
  'y+1/2, -z+1/2, x'
  'y+1/2, -z+1/2, -x'
  '-y+1/2, z+1/2, x'
  '-y+1/2, -z+1/2, x'
  'y+1/2, z+1/2, -x'
  'y+1/2, x+1/2, -z'
  '-y+1/2, -x+1/2, z'
  '-y+1/2, -x+1/2, -z'
  'y+1/2, x+1/2, z'
  'y+1/2, -x+1/2, z'
  '-y+1/2, x+1/2, -z'
  '-y+1/2, x+1/2, z'
  'y+1/2, -x+1/2, -z'
  'x+1/2, z+1/2, -y'
  '-x+1/2, -z+1/2, y'
  '-x+1/2, z+1/2, y'
  'x+1/2, -z+1/2, -y'
  '-x+1/2, -z+1/2, -y'
  'x+1/2, z+1/2, y'
  'x+1/2, -z+1/2, y'
  '-x+1/2, z+1/2, -y'
  'z+1/2, y+1/2, -x'
  '-z+1/2, -y+1/2, x'
  'z+1/2, -y+1/2, x'
  '-z+1/2, y+1/2, -x'
  '-z+1/2, y+1/2, x'
  'z+1/2, -y+1/2, -x'
  '-z+1/2, -y+1/2, -x'
  'z+1/2, y+1/2, x'

loop_
  _atom_site_label
  _atom_site_occupancy
  _atom_site_fract_x
  _atom_site_fract_y
  _atom_site_fract_z
  _atom_site_adp_type
  _atom_site_U_iso_or_equiv
  _atom_site_type_symbol
  Fe        0.3333  0.000000     0.000000     0.000000    Uiso  ? Fe
  Co        0.3333  0.000000     0.000000     0.000000    Uiso  ? Co
  Ni        0.3333  0.000000     0.000000     0.000000    Uiso  ? Ni
```

Note 2. FeCoNi contents from TGA

Given that the TGA of FeCoNi@HNC samples was conducted in the air, it is expected that FeCoNi alloy nanoparticles would be converted into oxides after the combustion of N-rich carbon matrices. Here we assumed that Fe, Co and Ni were oxidized into Fe_3O_4, Co_3O_4 and NiO, respectively. Since the mole ratio of Fe:Co:Ni in the alloy nanoparticles 1:1:1, the mass content of FeCoNi alloy nanoparticles in FeCoNi@HNC after acid etching was calculated as follows:

$$m(\mathrm{FeCoNi}) = m(\mathrm{FeCoNi\ oxides}) \times \frac{M_{Fe} + M_{Co} + M_{Ni}}{\frac{M_{\times Fe_3O_4}}{3} + \frac{M_{Co_3O_4}}{3} + M_{NiO}} \times 100\% \quad (13)$$

where m represents mass fraction, and M is molar mass. In Fig. 2b, m(FeCoNi oxides) = 37.69%. Therefore, m(FeCoNi) = 37.69%×(173.465/232.154) = 28.16%.

Similarly, for FeCoNi@HNC before acid etching, m(FeCoNi oxides) = 62.40% in Fig. S8, thus the mass content of FeCoNi alloy nanoparticles in the sample was calculated to be 46.63%.

4. Supplementary Tables

Table S1. Crystallographic data and structural refinements summary of FeCoNi@HNC.

Component	Space group	a (Å)	b (Å)	c (Å)	V (Å3)	R_{wp} (%)	R_p (%)
FeCoNi	Fm-3m	3.577696	3.577696	3.577696	45.794182	4.15	7.74
Graphite C	R3	2.459407	2.459407	3.370370	20.386299	4.15	7.74

Table S2. Comparison of the electrochemical performance of FeCoNi@HNC and other recently reported state-of-the-art binary TM@NC electrocatalysts in rechargeable zinc-air batteries.

Catalyst	ΔE^a (V)	Open-circuit voltage (V)	Power density (mW cm^{-2})	Stable cycle number (running time)	$\Delta\eta^b$ (V)	Ref.
FeCoNi@HNC	0.81	1.53	109.3	200 cycles (~67 h)	0.76	This work
NCNT/CoO-NiO-NiCo	0.77	1.30	-	100 cycles (~17 h)	0.86	[13]
N-GCNT/FeCo-3	0.81	1.48	89.3	240 cycles (40 h)	1.49	[14]
CoNi(1:1)-TB-800N_2	0.63	<1.30	154.8	34 cycles (136 h)	~0.6	[15]
NiFe@NBCNT	0.6	1.44	80	200 cycles (~130 h)	~0.8	[16]
$FeCu_{0.3}$-N/C	0.78	1.50	111	(75 h)	~1.1	[17]
1.5FeNi@NCT	0.60	1.44	114	100 cycles (~33 h)	1.1	[18]
CoFe@NP-CHS	0.67	1.516	123.1	120 cycles (40 h)	0.682	[19]
FeSb-N-CLs-50	~1.1	1.45	-	100 cycles (100 h)	0.94	[20]
FeCo@NC-750	0.69	1.38	132	120 cycles (20 h)	~0.86	[21]

CoNi/NCNSAs/CC-800	0.68	1.41	98.8	40 cycles (13.3 h)	0.66	[22]

[a] ΔE is the potential gap between OER potential at 10 mA cm^{-2} and ORR half-wave potential ($E_{1/2}$).

[b] Δη is voltage gap between the charging voltage platform and the discharging voltage platform.

5. Supplementary References

1. P. Yin, T. Yao, Y. Wu, L. Zheng, Y. Lin, W. Liu, H. Ju, J. Zhu, X. Hong, Z. Deng, G. Zhou, S. Wei and Y. Li, *Angew. Chem. Int. Ed.*, 2016, **55**, 10800−10805.
2. G. Kresse and J. Hafner, *Phys. Rev. B*, 1993, **47**, 558−561.
3. G. Kresse and J. Hafner, *Phys. Rev. B*, 1994, **49**, 14251−14269.
4. P. E. Blöchl, *Phys. Rev. B*, 1994, **50**, 17953−17979.
5. G. Kresse and D. Joubert, *Phys. Rev. B*, 1999, **59**, 1758−1775.
6. J. P. Perdew, K. Burke and M. Ernzerhof, *Phys. Rev. Lett.*, 1996, **77**, 3865−3868.
7. S. Grimme, *J. Comput. Chem.*, 2006, **27**, 1787−1799.
8. J. K. Nørskov, J. Rossmeisl, A. Logadottir, L. Lindqvist, J. R. Kitchin, T. Bligaard and H. Jónsson, *J. Phys. Chem. B*, 2004, **108**, 17886−17892.
9. H. Fei, J. Dong, Y. Feng, C. S. Allen, C. Wan, B. Volosskiy, M. Li, Z. Zhao, Y. Wang, H. Sun, P. An, W. Chen, Z. Guo, C. Lee, D. Chen, I. Shakir, M. Liu, T. Hu, Y. Li, A. I. Kirkland, X. Duan and Y. Huang, *Nat. Catal.*, 2018, **1**, 63−72.
10. X. Liu, Y. Jiao, Y. Zheng, K. Davey and S.-Z. Qiao, *J. Mater. Chem. A*, 2019, **7**, 3648−3654.
11. D. Xu, X. Long, Juanxiu Xiao, Z. Zhang, G. Liu, H. Tong, Z. Liu, N. Li, D. Qian, J. Li and J. Liu, *Chem. Eng. J.*, 2021, **422**, 129982.
12. Y. Li, H. Su, S. H. Chan and Q. Sun, *ACS Catal.*, 2015, **5**, 6658−6664.
13. X. Liu, M. Park, M. G. Kim, S. Gupta, G. Wu and J. Cho, *Angew. Chem. Int. Ed.*, 2015, **54**, 9654−9658.
14. C.-Y. Su, H. Cheng, W. Li, Z.-Q. Liu, N. Li, Z. Hou, F.-Q. Bai, H.-X. Zhang and T.-Y. Ma, *Adv. Energy Mater.*, 2017, **7**, 1602420.
15. X. He, F. Yin, G. Li, B. Chen, S. Wang and M. Gu, *J. Mater. Chem. A*, 2020, **8**, 25805−25823.
16. D. Bin, B. Yang, C. Li, Y. Liu, X. Zhang, Y. Wang and Y. Xia, *ACS Appl. Mater. Interfaces*, 2018, **10**, 26178−26187.

17. B. Wang, L. Xu, G. Liu, Y. Ye, Y. Quan, C. Wang, W. Wei, W. Zhu, C. Xu, H. Li and J. Xia, *J. Alloys Compd.*, 2020, **826**, 154152.
18. M. Wu, B. Guo, A. Nie and R. Liu, *J. Colloid Interface Sci.*, 2020, **561**, 585−592.
19. H.-J. Niu, S.-S. Chen, J.-J. Feng, L. Zhang and A.-J. Wang, *J. Power Sources*, 2020, **475**, 228594.
20. J.-C. Liang, K.-Y. Zhou, G.-Y. Chen, W.-X. Zhang, J.-A. Liu, W.-Z. Zhang, Z.-P. Zhang, W. Hou, M. Zhou, G.-F. Liu and F. Niu, *J. Solid State Electrochem.*, 2017, **21**, 3315−3324.
21. P. Cai, S. Ci, E. Zhang, P. Shao, C. Cao and Z. Wen, *Electrochim. Acta*, 2016, **220**, 354−362.
22. W. Zhang, Z. Li, J. Chen, X. Wang, X. Li, K. Yang and L. Li, *Nanotechnology*, 2020, **31**, 185703.